Ceramics International 51 (2025) 19485–19496

Contents lists available at ScienceDirect

Ceramics International

journal homepage: www.elsevier.com/locate/ceramint

High-temperature tribological properties of tungsten carbide reinforced high-entropy-alloy composite coating by laser cladding

Wenxing Wu [a,1], Hanxia Liu [b,1], Xuming Jin [c], Liangliang Guo [c], Tao Zhu [c], Liangbin Hu [c], Chao Yang [d,*], Pinghu Chen [c,**], Changjun Qiu [c], Paul K. Chu [e]

[a] College of Nuclear Science and Technology, University of South China, 421001, Hengyang, China
[b] School of Electrical Engineering, University of South China, 421001, Hengyang, China
[c] Key Laboratory of Hunan Province of Equipment Safety Service Technology Under Extreme Environment, College of Mechanical Engineering, University of South China, 421001, Hengyang, China
[d] National Engineering Research Center of Light Alloy Net Forming, School of Materials Science and Engineering, Shanghai Jiao Tong University, Shanghai, 200240, China
[e] Department of Materials Science & Engineering, City University of Hong Kong, Tat Chee Avenue, Kowloon, 999077, China

ARTICLE INFO

Handling Editor: Dr P. Vincenzini

Keywords:
Laser cladding (A. Processing)
Composite (B. Structure and Microstructure)
Carbides (D. Compositions)
Wear resistance (C. Properties)
Wear parts (E. Applications)

ABSTRACT

To solve the serious wear problem of mold steels at a high temperature, a 15 wt% WCp (Tungsten Carbide particles) reinforced $Fe_{50}Mn_{30}Cr_{10}Co_{10}$ HEA (High Entropy Alloy) composite coating is fabricated by laser cladding to improve the high-temperature wear resistance based on high hardness and thermal stability of HEA. Tribological tests are carried out at different temperature, and the wear mechanism is explored. The experimental results reveal three main phases of γ-Fe, WC, and W_2C in the LCed (Laser Cladded) HEA composite coating. Small amounts of nanoscale WC and MnO are precipitated to enhance the mechanical properties. The variation rule pertaining to the volume wear rate is that the values rise first and fall later with increasing temperature. The maximum wear rate is observed above 5×10^{-5} $mm^3/N{\cdot}m$ at 400 °C. Although the hardness may diminish with increasing temperature in theory, the relative wear resistance can be improved because the oxide could enhance the supportive capacity and isolating effects of the glaze layer between the friction pair. Fe_2O_3 can be considered a solid lubricant to reduce the wear rate. With increasing friction temperature, the wear mechanism changes from typical abrasive/fatigue wear to adhesive/delamination wear. Consequently, the 15 wt % WCp-reinforced HEA composite shows excellent wear resistance at 800 °C relative to H13 steel and the results provide the theoretical and experimental basis for liquid die forging.

1. Introduction

Liquid die forging (squeeze casting), a green forming technology for metal parts, has the advantages of conventional casting and forging techniques [1–3]. it can contribute to high quality of the products, including excellent mechanical properties, intricate shape, and good surface quality [4–6]. As a consequence, it has been used to manufacture important structural components with low melting point (Al alloy or its composites) in the automobile and aerospace industries [7,8]. However, the industry requires a wide range of materials, from lightweight alloys to high-strength alloys with a high melting point and high hardness [9–12]. Forging die can be considered as a component contacted with high-hardness forgings, in which suffers from serious wear and plastic deformation under the conditions of high temperature and high pressure. For H13 die steel, H13 steel has a high wear rate with $795.18 \pm 16 \times 10^{-6}$ $mm^3/N{\cdot}m$ at room temperature when its value is $36.13 \pm 0.72 \times 10^{-6}$ $mm^3/N{\cdot}m$ at 800 °C [13]. Consequently, relatively poor product quality and productivity, short service lifetime, or high remanufacturing cost can be caused [14–16]. Therefore, higher-performance surface materials of forging die should be prepared to resist the damage.

Wear-resistant coating is a most efficient method to improve the reliability and service life of the forging die. These technologies mainly include Physical Vapor Deposition (PVD) [17], Chemical Vapor Deposition (CVD) [18], plasma spraying [19], laser cladding [20] and so on.

* Corresponding author.
** Corresponding author.
E-mail addresses: wuzhiaifrank@hotmail.com (W. Wu), libraxia@163.com (H. Liu), chaoyang0315@163.com (C. Yang), chenpinghu1986@163.com (P. Chen).
[1] First authors.

https://doi.org/10.1016/j.ceramint.2025.02.124
Received 14 August 2024; Received in revised form 23 January 2025; Accepted 10 February 2025
Available online 14 February 2025
0272-8842/© 2025 Elsevier Ltd and Techna Group S.r.l. All rights are reserved, including those for text and data mining, AI training, and similar technologies.

Cathodic Arc-PVD is employed to prepare TiCrN/DLC (Diamond-like Carbon) coatings on D3 tool steel, the service life of TiCrN/DLC coatings is 2 times higher than that of uncoated dies [21]. In addition, the hybrid method with PVD and plasma nitride is designed to prepare a hybrid layer, a non-stoichiometric chromium nitride with higher hardness contributes to better wear resistance enhanced by 80 % relative to single nitrided coating for the forging tool die [17,22]. An excellent wear-resistant coating with low COF (Coefficient of Friction) has been prepared by PVD/CVD (Chemical Vapor Deposition) for steel dies in Al high-pressure die casting (HPDC), a below 0.4 COF and 10^{-8} mm^3/N·m wear rate are discovered, in which minimizing the chemical and mechanical degradation [23]. Globular larger size carbides are formed after 600 °C to improve hardness and wear resistance of the surface, but the cavitation erosion cannot be improved for high velocity air fuel spraying (HVAF)/high velocity oxygen fuel spraying (HVOF) tool steel [24]. A high-hardness stellite 6 coating has been deposited by the Gas Tungsten Arc Cladding (GTAC) process, effect of heat inputs on hardness and surface morphology is discussed, hardness is increased, but cold cracks emerge [25]. A Cr_3C-NiCr coating with a hardness of 830 HV has been plasma-sprayed successfully onto H13 tool steel, the enhancement in wear resistance of Cr_3C-NiCr coating occurs and 3 times higher than that of H13 steel, this can be because that Cr and Ni oxides contribute to the lower COF and wear rate [13]. However, PVD/CVD has a relatively low deposition efficiency when plasma spraying has a low utilization rate and powder contamination [26,27]. Laser additive manufacturing is one of the most effective methods for preparing wear-resistant coatings due to the good metallurgical bond with the substrate caused by higher temperature relative to the melting point [28,29]. The plasma-transferred arc direct energy deposition (PTA-DED) technique is employed to manufacture ceramic-reinforced composite coatings on the surface of 90MnCrV8 cold work tool steel, the particles(*in situ* ceramic FeW, B_4C, and TiB_2)-reinforced coating has a strong bonding with the substrate without defects, cracks, and gaps, so the wear resistance of enhanced coatings is 5–9 times higher than that of tool steel due to the high hardness (1.4–4.7 times relative to the substrate) and relatively small COF (03-0.6) [30]. CoCrCuFeNiTix HEA coatings are synthesized by laser cladding to prolong the service life. The hard phases precipitate and grains are refined because of Ti addition, the maximum hardness exceeds 550 HV in $Ti_{1.5}$ coating. The TiO_2 layer formed at 600 °C, the average friction coefficient decreases from 0.54 of 45 steel to 0.15 of $Ti_{1.5}$ coating, in which results in weakening abrasion and oxidative wear [31]. However, different materials show different oxidation and wear mechanisms at high temperatures, especially multi-component high entropy alloys (HEA) [32,33].

$Fe_{50}Mn_{30}Cr_{10}Co_{10}$ HEA, a typical material, has an excellent combination properties of high strength-ductility, good corrosion resistance and heat stablity because of TRIP effect caused by dual phase with FCC and HCP structures [34–36]. Meanwhile, it has a good high-temperature oxidation resistance owing to a continuous Cr-rich oxide layer [35]. There are a huge modification space for special properties via ajusting the ratio of the phase, but the hardness about 208 $HV_{0.2}$ is relatively insufficient [37], resulting in low wear resistance. For this purpose, the addition of V element and post heat treatment can contribute to the formation of BCC particles and higher ratio of ε-martensite laths, which enhance the hardness [38]. A higher hardness was exhibited caused by the lattice distortion and the presence of Al-rich brittle intermetallic compounds (IMCs) owing to the addition of high-ratio Al [39]. Furthermore, TiB2 and Mo can be contribute to higher microhardness and wear resistance caused by the formation of a clustered microstructure with σ and TiB_2 phases [40]. In our previous work, influence of different WC particles content on hardness and wear resistance is studied in Ref. [41]. Relative wear resistance of 15–20 wt% WCp/HEAs exceeds from 4 times to 62 times for H13 steel [13,42]. However, high-temperature oxidation and wear mechanism of WCp reinforced $Fe_{50}Mn_{30}Cr_{10}Co_{10}$ HEA composite is not well known. In light of this, to clarify the wear mechanism of WCp reinforced HEA composite at high temperature condition. A 15 wt% tungsten carbide reinforced $Fe_{50}Mn_{30}Cr_{10}Co_{10}$ HEA is prepared by laser cladding. The microstructure and phase constituents are characterized by XRD, SEM, EBSD, and TEM and the tribological properties are determined at different temperatures with room temperature, 400 °C, 600 °C, and 800 °C. Moreover, the wear mechanism is explored in depth.

2. Experimental details

The commercial $Fe_{50}Mn_{30}Cr_{10}Co_{10}$ high-entropy-alloy (HEA) powder was supplied by Ningbo Zhongyuan Advanced Materials Technologies Co., Ltd. Tungsten carbide particles were provided by Shanghai Puwei Applied Materials Technology Co., Ltd. Their detail information about elemental ratio, particle size and micro-morphology has been described in Ref. [41]. The two mixed powders with 85 wt% HEA and 15 wt% tungsten carbide were prepared using the QM-3SP04 ball mill, supplied by Beijing Beituo Instrument Equipment Co., Ltd., which was operated at a speed of 20 r/min for 120 min. The microstructure and phase of the mixed powders are shown in Figs. 1 and 2. The tungsten-carbide powders were uniformly distributed in the HEA powders. According to the XRD pattern of the mixed powders, the HEA powders (88–2323) had the γ phase with face-centered cubic (fcc) structure. Tungsten carbide included W_2C (35–0776) and WC (72–0097) with (101) crystallographic planes at 39.6° and 48.3°, respectively.

A fiber laser welding machine (XL-F1000, Guangzhou Xinlai Laser Technology Co., Ltd., Guangzhou, China) with a 1000 W continuous wave laser at a wavelength of 1080 nm was utilized to fabricate the 15 wt% tungsten carbide reinforced HEA samples, as shown in Fig. 3(a) and (b). For process parameters, laser power of 450~650 W, scanning rate of 400~900 mm/min, overlapping rate of 0~70 % and powder delivery of 8~12 g/min were optimized through a comparison of the deposition rate, samples' quality and mechanical properties. Ultimately, the optimized laser parameters were determined for laser power of 550 W, scanning rate of 550 mm/min, overlapping rate of 50 %, and powder delivery rate of 10 g/min 99.99 % pure Ar was the shielding gas, and the flow rate was 14 L/min to prevent air from entering the molten pool. The mixed powders were laser-cladded on the surface of the Q235 steel plate with dimensions of 100 mm × 50 mm × 15 mm. Some rectangular samples with dimensions of 30 mm × 30 mm × 5 mm were fabricated by the "stripe" scanning strategy using a rotation angle of 90° between adjacent layers. According to Fig. 3(c), the surface of the original samples was smoothed by grinding. Afterward, the specimens were cut into pieces with sizes of 10 mm × 10 mm × 5 mm and 20 mm × 20 mm × 5 mm.

The dry friction tests were performed on the high-temperature friction-wear machine (HT-1000, Zhongke Kaihua, Lanzhou, China), as shown in Fig. 3(d). Before the dry friction tests, the specimens were polished with different grit sandpapers. Some parameters in the friction test were programmed for a friction force of 20 N, rotation speed of 500 r/min, friction radius of 4 mm, and friction time of 30 min. A Si_3N_4 ball was the counterpart. The friction properties were determined at room temperature (RT), 400 °C, 600 °C and 800 °C. The comparison experiments of friction test were adopted on the H13 steel under the same conditions. The volume wear rate was calculated by $w = V/(L{\cdot}F)$ [43], where w represents the volume wear rate, $mm^3/(m{\cdot}N)$, V is the wear volume equal to 2πr × wear area, mm^3, L is the total distance equal to 2πr × v (rotation velocity) × t (friction time), m. and F is the friction force, N. For the accuracy of measured data, all friction test are repeatedly measured three times in different samples fabricated by the same assignment, the average wear area was calculated four times of each sample at quarter positions by 3D laser confocal scanning microscopy (VK-X200 series, Keyence Corporation of America). The 3D morphology and outline of the wear tracks were evaluated by the VK Analytics software.

To observe the microstructure and phase constituents, the specimens were polished with different grit sandpapers, followed by vibrational

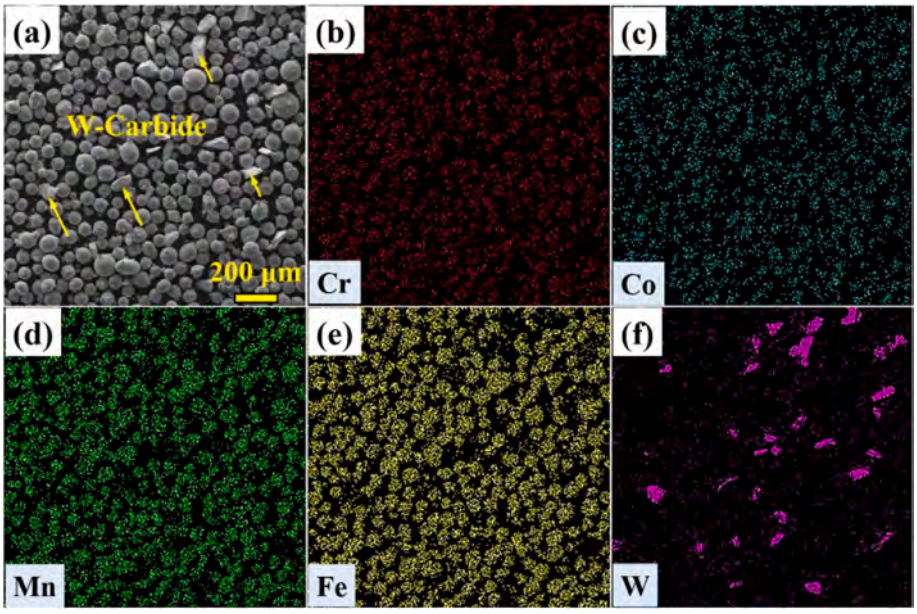

Fig. 1. SEM images and EDS elemental maps of the mixed powders with 15 wt% tungsten carbide.

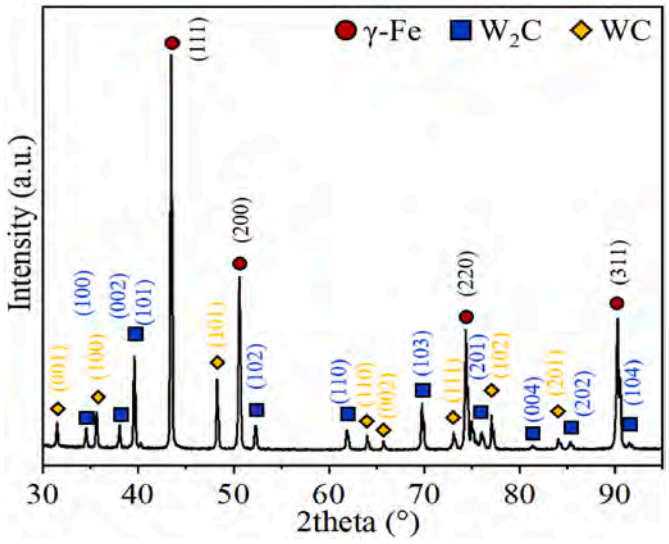

Fig. 2. XRD pattern of the mixed powders with 15 wt% tungsten carbide.

polishing with an amplitude of 60 μm for 7 h. High-energy X-ray diffraction (HE-XRD, D8 discover, Bruker, Germany) was utilized to examine the phases of the mixed powders and the surface of the wear tracks after the friction-wear tests at different temperatures using Cu K_α radiation ($\lambda = 0.15418$ nm) at 45 kV and 150 mA in the 2-theta range of 30–95° and a scanning rate of 3°/min. The EBSD information of the inverse pole figure (IPF), pole figure (PF), grain size, and disorientation angle was acquired by electron back-scattered diffraction (EBSD, FE-SEM (Carl Zeiss, SUPRA®55, Germany)) on the FEI SCIOS focused ion beam scanning electron microscope at 15 keV voltage and 12 nA probe current with the Hikari camera and TSLOIM data-collection software. To explore the sub-crystal structure, transmission electron microscopy (TEM, JEM-3200FS, JEOL, Japan) was employed to acquire the high-resolution TEM image and electron diffraction patterns. The TEM sample was ground to a thickness below 100 μm, and then a wafer with φ of 3 mm was prepared. An ion milling system was used at a beam voltage of 4 kV and milling angle of 4° to satisfy the thickness requirement for TEM.

3. Results and discussion

The SEM images of the cross-section of the laser-cladding sample are shown in Fig. 4. The tungsten carbide particles have a relatively uniform distribution and mitigate serious wear. A good bond is formed between tungsten carbide and HEA due to elemental diffusion caused by the high temperature during laser cladding. Therefore, there is a mixed transition region at the interface, as shown in Fig. 4(b) and (c). The new precipitate is converted into a W intermetallic compound. In addition, excellent metallurgical bonding is shown in Fig. 4(d), and W diffuses into the HEA matrix. The contrast of the W precipitate decreases gradually from the HEA composite coating to the substrate. The result is consistent with the elemental line scans in Fig. 4(e). The OM images of the cross-section are acquired after metallographic etching with aqua regia. The cross-section can be divided into three regions: clad layer (HEA composite coating), transition layer (heat-affected zone), and substrate, as shown in Fig. 5 (a). The OM images of six zones are obtained by OM, which reveals that small cells and columnar crystals exist simultaneously at the boundary of the molten pool, as shown in Fig. 5(c). Meanwhile, the bulky dual-phase structure and fine equiaxed crystals are formed in the transition layer because of the larger heat gradient, as shown in Fig. 5(e) and (f).

Fig. 6 shows the EBSD results of tungsten carbide-reinforced HEA, in which tungsten-carbide particles are distributed uniformly (Fig. 6(a)). Meanwhile, fine grains with ~50 μm are surrounded by coarse grains with a length of 500 μm and width less than 100 μm. Fine grains mainly exist at the junction between two tracks because nucleation in the overlapping zone inhibits the epitaxial growth of equiaxed grains [44]. As shown in Fig. 6(d), the ratio of low-angle grain boundaries (LAGB, <15°) is about 49 %, which is less than that of high-angle grain boundaries (HAGB, >15°), as shown in Fig. 6(d)–(e). The HAGB is mainly distributed within 60°. The LAGB and HAGB are largely concentrated in the fine-grain region on account of high-density dislocations caused by local stress during solidification [45]. According to IPF and PF images, an obvious preferred growth orientation cannot be identified from the HEA matrix as the intensity is below 2.6 in Fig. 6(g).

The microstructure is further examined by TEM, as shown in Fig. 7. The high temperature and rapid cooling can exist during laser cladding owing to high energy density [31], a relatively large molten pool can extend its solidification and cool time, moreover, higher overlap rate can be contribute to re-melting the previous track, which resulting in the reduction of cooling rate [46]. Enough time is supplied to decompose

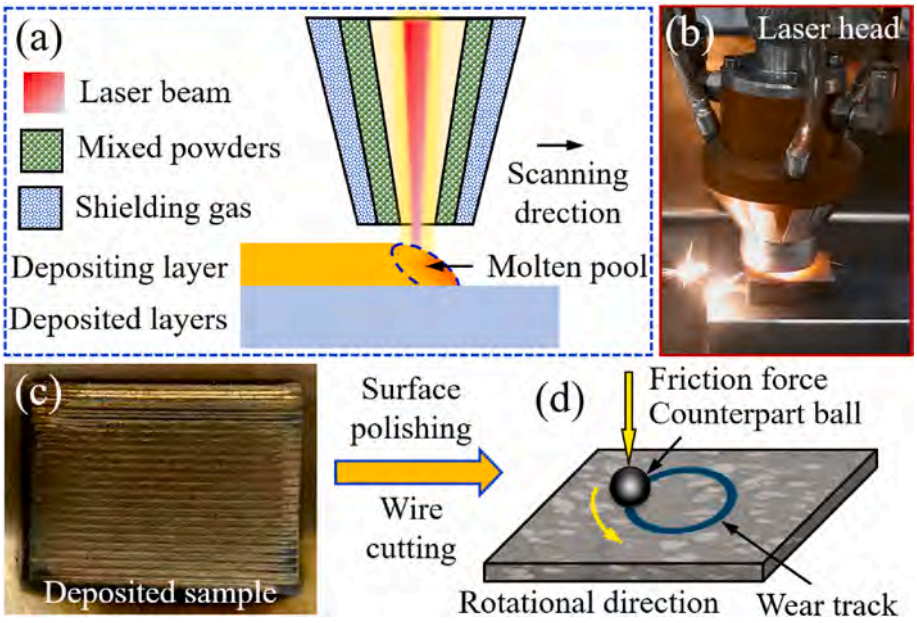

Fig. 3. (a) Schematic diagram, (b) Real laser head of laser cladding, (c) Deposited sample, and (d) Schematic diagram of the friction test.

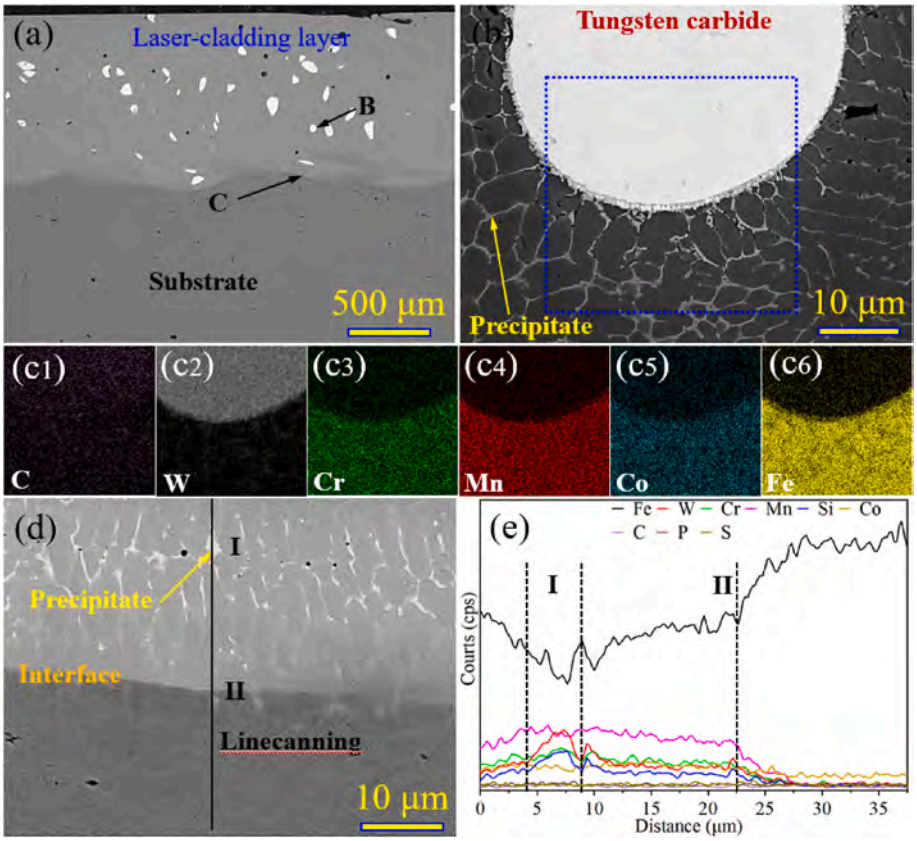

Fig. 4. SEM images and EDS elemental maps of the cross-section of the as-fabricated sample. (a) Low-magnification image, (b) High-magnification image of the interface between tungsten carbide and HEA, (c) SEM-EDS mapping images of alloying elements in (b), (d) High-magnification image of the interface between the laser-cladding composite coating and substrate, and (e) Elemental concentration line scans in (d).

the original tungsten carbide within the HEA matrix. A portion of the W and C interstitial solutes is incorporated into the FCC structure, and another part contributes to the *in situ* formation of fresh tungsten carbide [47]. The precipitated tungsten carbides have a discontinuous net-like and sub-micron granular structure, see Fig. 7(a)–(c). Especially, MnO can be formed owing to O solid solution formed by laser cladding [48]. Observing the black region at high-magnification, and the corresponding EDS elemental analysis of A and B regions is exhibited in Fig. 7(d), high-intensity W peak exists in black region identified as W-rich carbide using TEM analysis. In the sub-micron in-situ granular structure, good

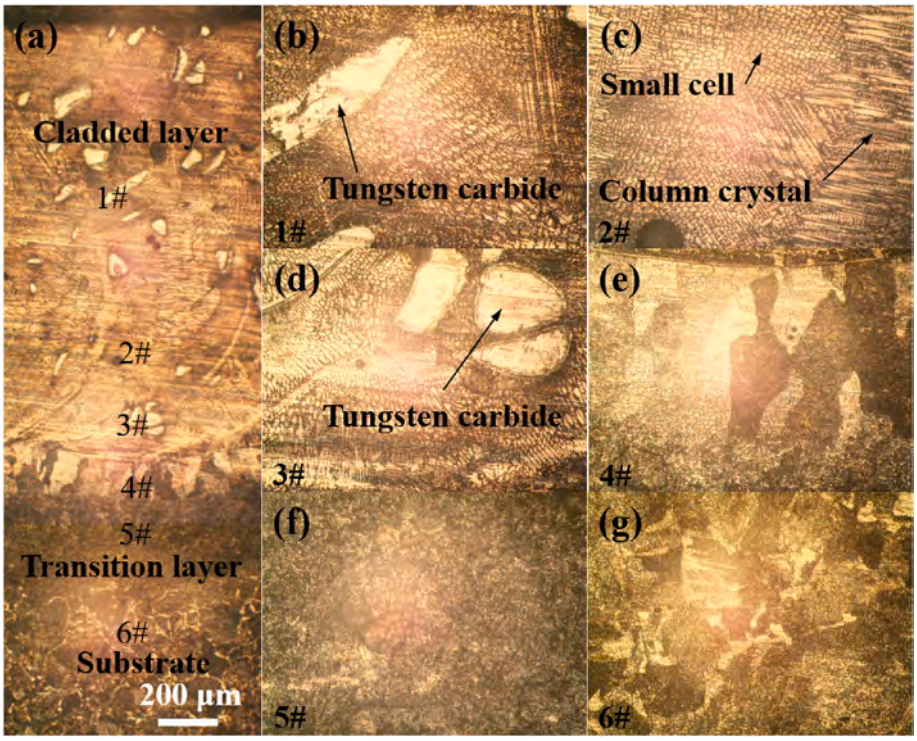

Fig. 5. OM images of the cross-section of laser-cladding sample. (a) Low-magnification image of the cross-section, (b) 1# region in (a), (c) 2# region in (a), (d) 3# region in (a), (e) 4# region in (a), (f) 5# region in (a), and (g) 6# region in (a).

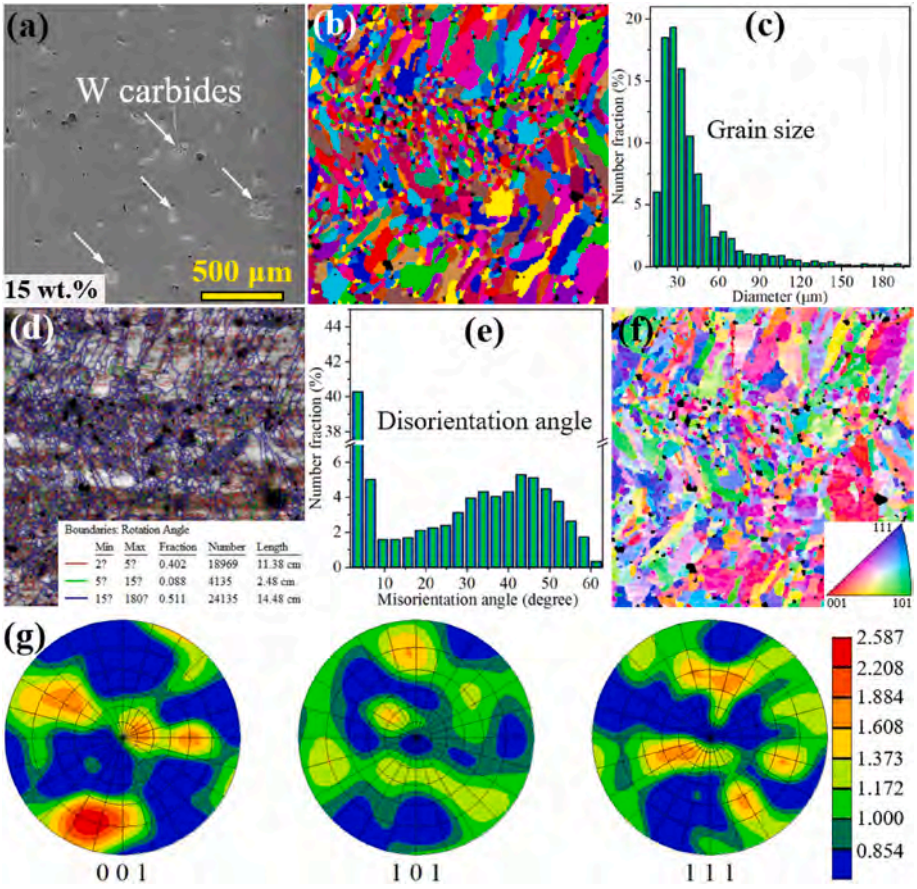

Fig. 6. EBSD image of the surface of as-fabricated sample. (a) SEM image, (b) Unique grain color, (c) Grain Size, (d) Disorientation angle, (e) IQ image, (f) IPF image, and (g) PF images. (For interpretation of the references to color in this figure legend, the reader is referred to the Web version of this article.)

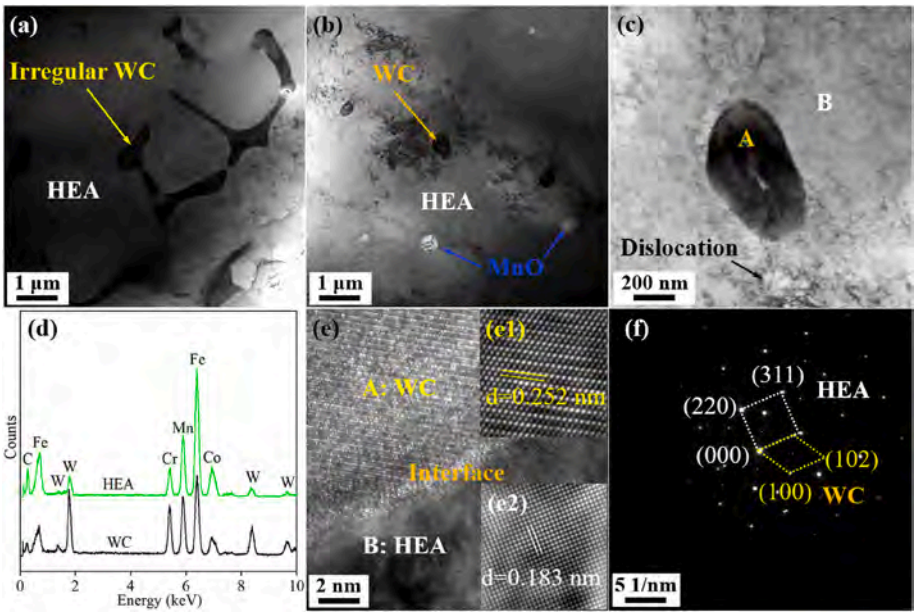

Fig. 7. TEM images and electron diffraction spots of the as-fabricated sample. (a) Precipitated discontinuous WC, (b) Sub-micron WC and MnO, (c) High-magnification WC, (d) EDS curves of WC particle and HEA matrix, (e) High-resolution images for WC and HEA matrix, (f) Electron diffraction pattern of the interface of WC and HEA.

bonding is formed at the interface between tungsten carbide and the HEA matrix, as shown in Fig. 7(c). The interplanar spacings of the tungsten carbide and HEA matrix in Fig. 7(e) indicate that tungsten carbide and the HEA matrix have the WC and FCC structure, they have the orientation relationship of $[1\text{-}1\text{-}2]_{HEA}//[0\text{–}10]_{WC}$, as shown in Fig. 7 (f). It can demonstrate furtherly that better bonding appears in the interface between the WC and HEA matrix.

The mechanical properties of the materials depend mainly on their

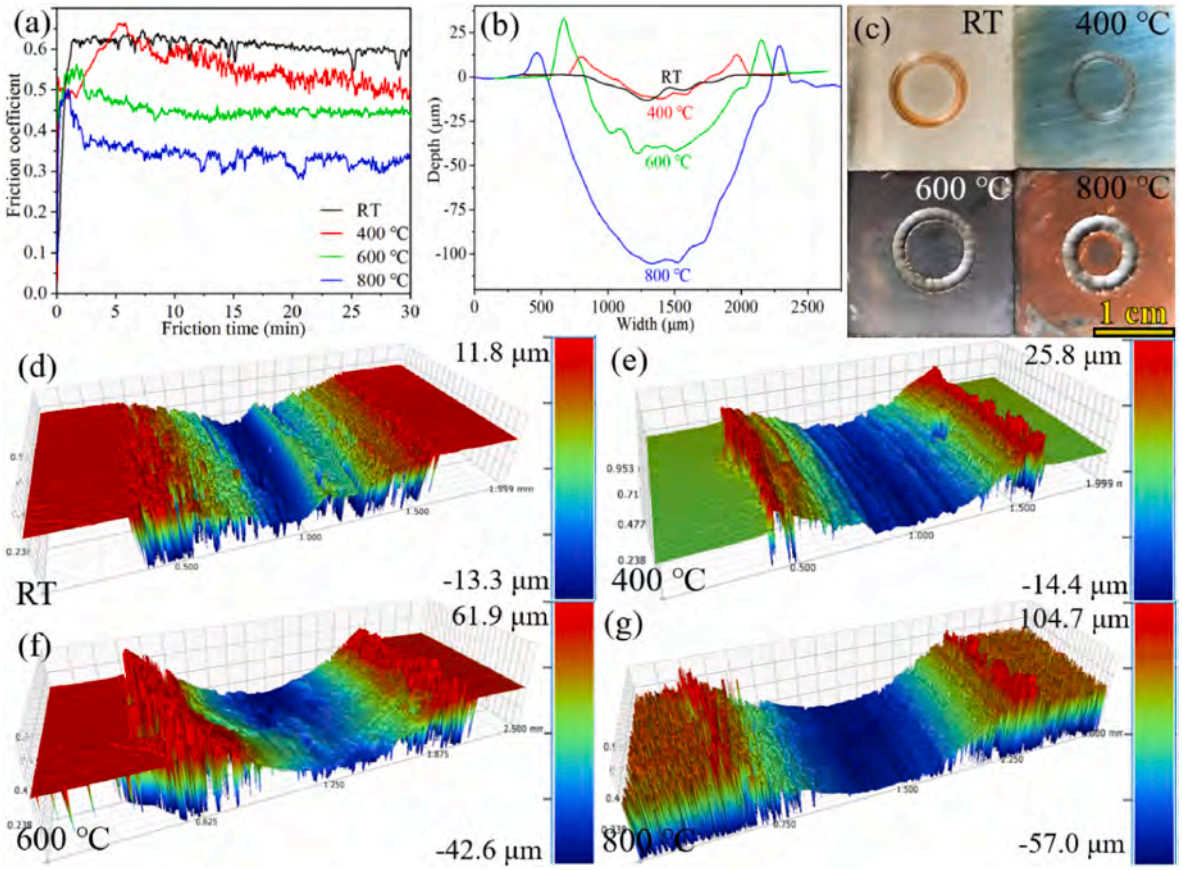

Fig. 8. Tribological characteristics of H13 steel at different temperature. (a) Friction coefficients, (b) Outlines of wear tracks, (c) Macro morphology at different temperature, (d) 3d morphology of wear tracks at RT (d), 400 °C (e), 600 °C (f), and 800 °C (g).

microstructure. The tribological properties of H13 steel and WCp/HEA composite coating at different temperatures are shown in Figs. 8 and 9 and Table .1. Fig. 8 shows tribological characteristics of H13 steel, friction coefficient (COF) of H13 steel is exhibited in Fig. 8(a), the relatively stable occurs at the entire stage, it can find that average COF is about 0.61 at the room temperature. But a relatively big fluctuation at other specific temperature. According to Table 1, average friction coefficient of H13 steel is gradually decreased with increasing friction temperature, average COF drops to 0.33 at 800 °C. Nevertheless, it is worth noting that lower COF did not reduce volume wear rate for H13 steel, just as Fig. 8(b), the outline of wear track at different temperature indicates that the width and depth has a gradually climbing trend with increasing friction temperature. Based on the measurement from local 3D graphs, the width of wear tracks first decreases and then increases, average width is only 1150 μm at 400 °C when the value exceeds 1910 μm at 800 °C. And the depth of wear tracks is increased markedly from 17.8 μm at room temperature to 108.8 μm at 800 °C. Meanwhile, macromorphology and 3D morphologies are showed in Fig. 8(c)–(g), the wear rate is dramatically increased with increasing friction temperature. The values show a sharp increase from 2.55 × 10^{-4} mm^3/N·m at room temperature to 42.88 × 10^{-4} mm^3/N·m at 800 °C, the detail data is showed in Table 1.

Nevertheless, an almost contrary tendency is displayed for WCp/HEA composite coating, the change in the volume wear rate increases initially but declines afterward. The worst wear exceeding 5 × 10^{-5} mm^3/N·m is observed at 400 °C. However, excellent wear resistance is observed at 800 °C, and the relative wear resistance is 2 times higher than that at 400 °C. Observing the COF versus temperature, as shown in Table 1 and Fig. 9(a). The COF at room temperature, 400 °C, 600 °C and 800 °C are 0.66, 0.29, 0.24 and 0.44, respectively. combine with the corresponding outline and 3D morphologies of the wear tracks (Fig. 9 (b1)-(f)). Fig. 9(b) shows the outline of the wear tracks at different temperatures, which are in accordance with the tendency of the volume wear rate. Meanwhile, local 3D graphs show a large disparity in the

Table 1
Tribological results of H13 and HEA composite coating at different temperature.

Sample No.	H13 steel		HEA composite coating	
	Average COF	Average wear rate (× 10^{-4} mm^3/N·m)	Average COF	Average wear rate (× 10^{-5} mm^3/N·m)
RT	0.61	2.55	0.66	2.09
400	0.53	3.96	0.29	5.18
600	0.45	16.4	0.24	1.81
800	0.33	42.88	0.44	1.3

surface features, towering plateaus emerge on the surface at 800 °C due to various degrees of high-temperature oxidation, as shown in Fig. 9. Compared with H13 steel, relative wear resistance of WCp/HEA composite coating is 7.4 times higher than that of H13 steel at room temperature when 328.8 times occurs at 800 °C. It indicates that excellent wear resistance of WCp/HEA composite coating at high temperature relative to H13 steel. Here a comparison in tribological characteristics are also discussed in Table .2, a relative superiority of this work is still exhibited in Table 2, especially at high temperature condition within the range of 600–800 °C.

According to the surface morphology, obvious oxides are not discovered below 600 °C, indicating that the WCp-reinforced HEA has excellent oxidation resistance below 600 °C, but a large amount of the oxide is found at 800 °C. Furthermore, the wear tracks are different at different temperatures. At room temperature, free debris exists in the wear tracks from serious wear, but the WC particles restrict the wear progress. The debris gathers around the WC particles. In the subsequent friction process, the debris is compacted to form a glaze layer, as shown in Fig. 10A1. The magnified image in Fig. 10A2 reveals WC particles in the dark-gray zone. With increasing friction time, fatigue cracks and delamination are observed from the glaze layer [55]. When the temperature goes up to 400 °C, serious plastic deformation contributes to

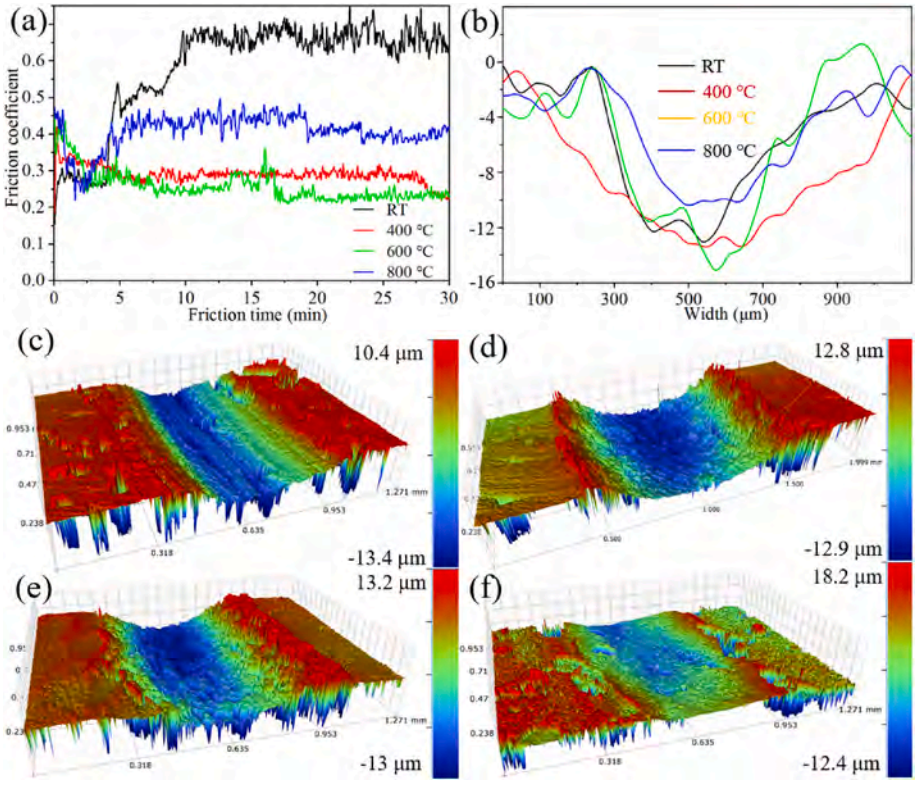

Fig. 9. Friction coefficients and wear characteristics of at elevated temperature. (a) Friction coefficients, (b) outlines of wear tracks, and local 3D morphology at (c) Room temperature, (d) 400 °C, (e) 600 °C, and (f) 800 °C.

Table 2
A comparison in tribological characteristics between this work and other WC-HEA composites.

Materials	Fabricated method	Volume wear rate	Reference
AlCoCrFeNiSi-10WC AlCoCrFeNiSi-20WC	high-velocity arc spraying	6.07×10^{-5} mm^3/N·m at RT 5.18×10^{-5} mm^3/N·m at RT	[49]
AlCoCrFeNiTi$_{0.5}$-10WC AlCoCrFeNiTi$_{0.5}$-20WC	laser cladding	2.4×10^{-5} mm^3/N·m at RT 1.9×10^{-5} mm^3/N·m at RT	[50]
CoCrFeNiMn-20WC	induction cladding	~25×10^{-5} mm^3/N·m at RT	[51]
CoCrFeNiMo$_{0.2}$Nb$_{0.2}$-10WC CoCrFeNiMo$_{0.2}$Nb$_{0.2}$-30WC	laser cladding	5.6×10^{-5} at 600 °C 8.15×10^{-5} at 800 °C 2.16×10^{-5} at 600 °C 4.28×10^{-5} at 800 °C	[52]
FeCrNiMnAl-15WC	laser cladding	1.846×10^{-5} mm^3/N·m at RT	[53]
FeCoCrNiMn-80WC	plasma cladding	750 μm in width and 12.5 μm in depth at 600 °C	[54]
Fe50Mn30Co10Cr10-15WC	laser cladding	2.09×10^{-5} mm^3/N·m at RT 5.18×10^{-5} mm^3/N·m at 400 °C 1.81×10^{-5} mm^3/N·m at 600 °C 1.3×10^{-5} mm^3/N·m at 800 °C	This work

plowing wear, as shown in Fig. 10B2. Meanwhile, brittle fracture can be caused by the stripping of WC particles. The area of the glaze layer increases with temperature to 600 °C, and fracture occurs at the edge of the glaze layer to form lamellar debris, as shown in Fig. 10C3. At 800 °C, serious oxidation is evident on the entire surface and is responsible for the unusual 3D confocal morphology. The surface of the debris is textured due to continuous oxidation, as shown in Fig. 10D.

The wear tracks are analyzed by HE-XRD, and the results are presented in Fig. 11. The XRD patterns at different temperatures are in line with the SEM observation. The phases include γ-Fe, WC, and W_2C when the temperature is below 400 °C. The formation of α-Fe_2O_3 [56] and MnO is initialed at 600 °C and accompanied by the original phases of γ-Fe, WC, and W_2C. The original phases are covered by the massive oxidation layer. Fe_2O_3, MnO, Cr_2O_3, and CoO are produced at temperatures below 800 °C, and this is the main reason why the volume wear rate and friction coefficient follow the specific trend with temperature.

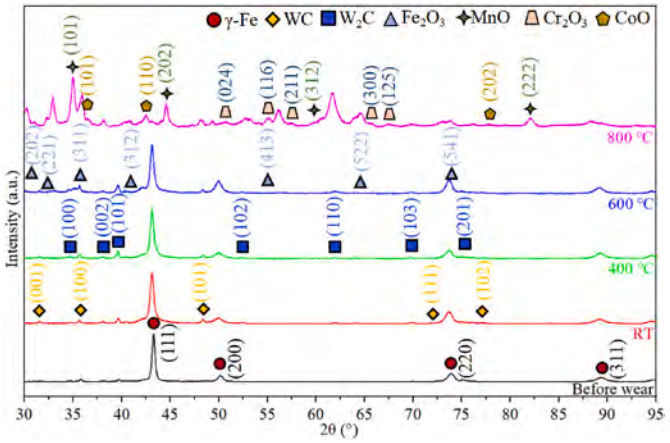

Fig. 11. XRD patterns after the wear test for different ambient temperatures.

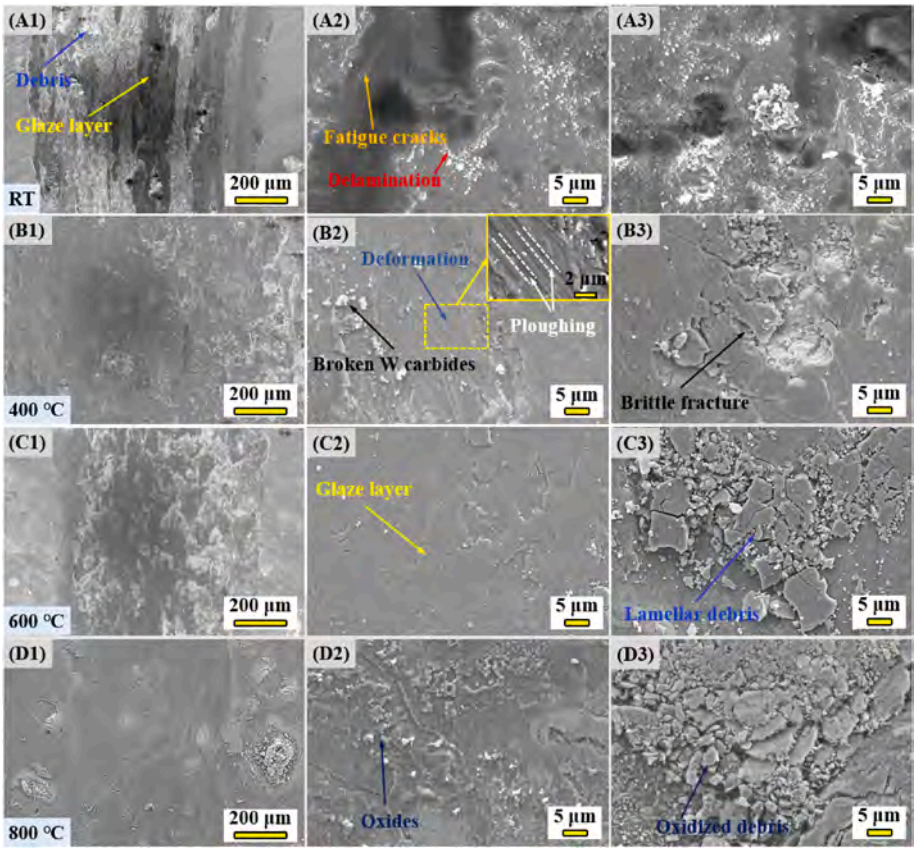

Fig. 10. SEM images of the wear tracks. (a) RT, (b) 400 °C, (c) 600 °C, and (d) 800 °C.

The morphology and elemental distribution of the wear track with the smallest volume wear rate are shown in Figs. 12 and 13. Fig. 12(a) and (d) depict the surface morphology at a magnification of 200 × . Some debris exists on the surface of the wear track in a free state. Fig. 12 (b) shows the central area of the WC particle. The porous oxide layer (1#) is discovered at a magnification of 10,000 × . The lamellar debris with nanoscale oxide is superimposed at the edge of the glaze layer (2#), as shown in Fig. 12(c). Similarly, a denser glaze layer is shown in Fig. 12 (e) at 10,000 × . Meanwhile, fatigue cracks are formed due to friction. In the 4# region, Mn oxide reforms on the surface of the wear track on account of the strong oxygen affinity [57–59], and it is validated by the EDS elemental distributions in Fig. 13. The plateau mainly includes O and Mn, and other elements are absent from the region. The oxides contribute to the high hardness and supportive capability.

The excellent wear resistance arises from two main factors, namely high hardness and small friction coefficient. Surface hardness is important to the supporting capability. In theory, the microhardness decreases with increasing temperature, thus resulting in a weak carrying capacity and serious wear [60,61]. The schematic diagram illustrating friction and wear at different temperatures is depicted in Fig. 14. In the composite, thick WC particles are embedded in the γ-Fe matrix and play a supportive role in withstanding a relatively large force [41]. However, the larger region contains a soft phase with the FCC structure and has weak wear resistance. Therefore, serious wear is observed at room temperature. The excellent oxidation resistance at 400 °C implies less oxide formation, thus hardly reflecting the strengthening effect. Materials like HEA and WC delaminate during the friction test and produce serious wear. Abrasive wear may be considered the typical wear mechanism, as shown in Fig. 14(b). However, at 600 °C, metal oxide particles are formed on the surface during the heating process to improve the average hardness, and Fe_2O_3 and MnO continue to grow during the friction test [62,63].

The oxides also play a supportive role in improving the hardness of the matrix [64,65]. Meanwhile, the soft exfoliated debris is flattened to form the glaze layer and isolate the mutual connection between the friction pair. In addition, Fe_2O_3 is a typical hard lubricant [63], and a low friction coefficient reduces the frictional resistance because of the weak obstacle against the relative motion between the kinematic pair. Consequently, the minimum friction coefficient is 0.24. The free debris and glaze layer contribute to the excellent wear resistance and create the phenomenon shown in Fig. 14(c) and (d). Consequently, a two-way wear mechanism consisting of abrasive and adhesive wear is observed at 600 °C. A large amount of oxide is formed on the surface when the temperature rises to 800 °C, as shown in Figs. 12 and 13. The enhanced hardness gives rise to a good wear resistance [65,66], but the friction coefficient picks up because Cr_2O_3 and CoO are formed at 800 °C. The friction coefficient of Cr_2O_3 decreases gradually with temperature, but still exceeds 0.4 [66]. The contact between the material surface and the counterpart ball is separated by a thicker oxidation layer. Most of the debris is compacted to form an extensive glaze layer, thus resulting in a lower volume wear rate and excellent wear resistance. According to the friction results, adhesive wear and delamination wear constitute the main mechanism at 800 °C, as shown in Fig. 14(e) and (f).

4. Conclusion

Laser cladding is employed to fabricate 15 wt% WCp-reinforced HEA composite coating. Friction and wear tests are performed at different temperature with the room temperature, 400, 600 and 800 °C. Wear mechanism is explored. The following are the main conclusions:

(1) The LCed HEA composite coating includes mainly phases of γ-Fe, MC, and M_2C carbides. Original tungsten carbides can be decomposed and then diffuse into HEA matrix, causing nanoscale precipitates due to the high temperature, large temperature gradient, and solidification rate in laser cladding.
(2) The HEA composite coating has an excellent high-temperature oxidation resistance below 600 °C. A small portion of Fe_2O_3 and MnO is formed at 600 °C, and Fe_2O_3 can be considered the solid lubricant phase to decrease friction. The average friction coefficient is 0.24 at 600 °C. However, Cr_2O_3 and CoO are also formed at 800 °C to increase the friction coefficient.
(3) Relative to H13 steel, wear resistance of composite coating is 7.4 times higher than that of H13steel at room temperature when 328.8 times occurs at 800 °C. The excellent wear resistance of composite coating stems from the synergistic effects of high surface hardness and small friction coefficient caused by WC particles and low COF oxides. With increasing temperature, the wear mechanism changes from abrasive/fatigue wear to adhesive/delamination wear.
(4) The formation of relatively abundant oxides can contribute to higher carrying capacity, the average volume wear rate is only

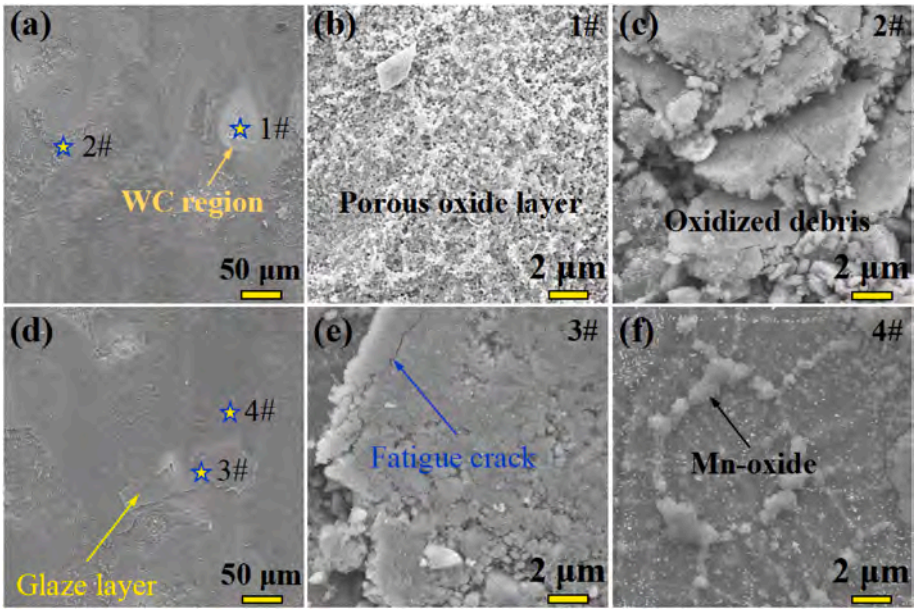

Fig. 12. SEM images of the wear track at 800 °C. (a and d) Low magnification images (200 ×), (b) 1# region, (c) 2# region, (e) 3# region, and (f) 4# region.

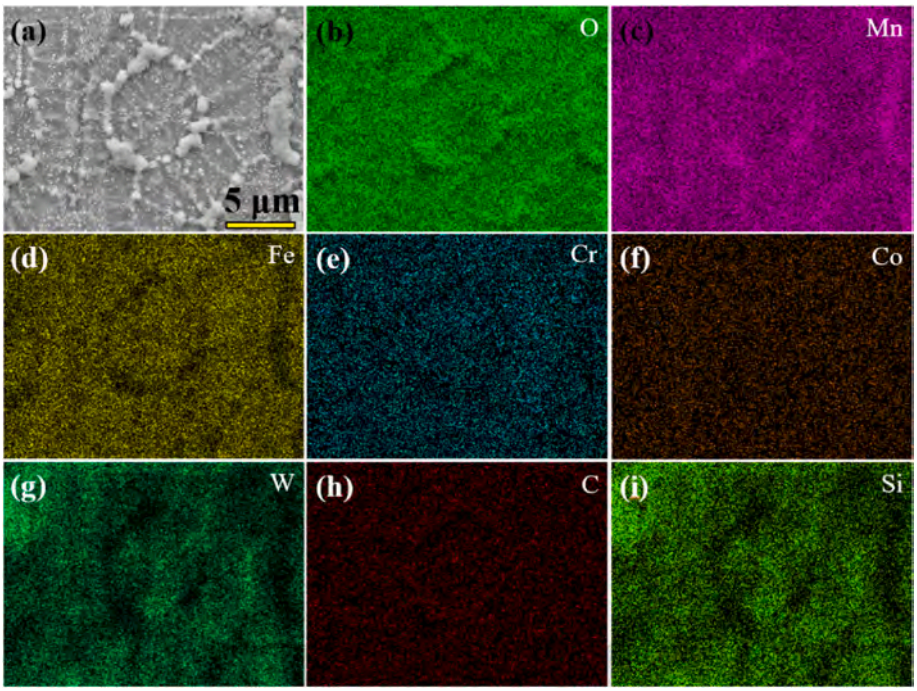

Fig. 13. EDS elemental maps of 2# region in the wear track shown in Fig. 12(f).

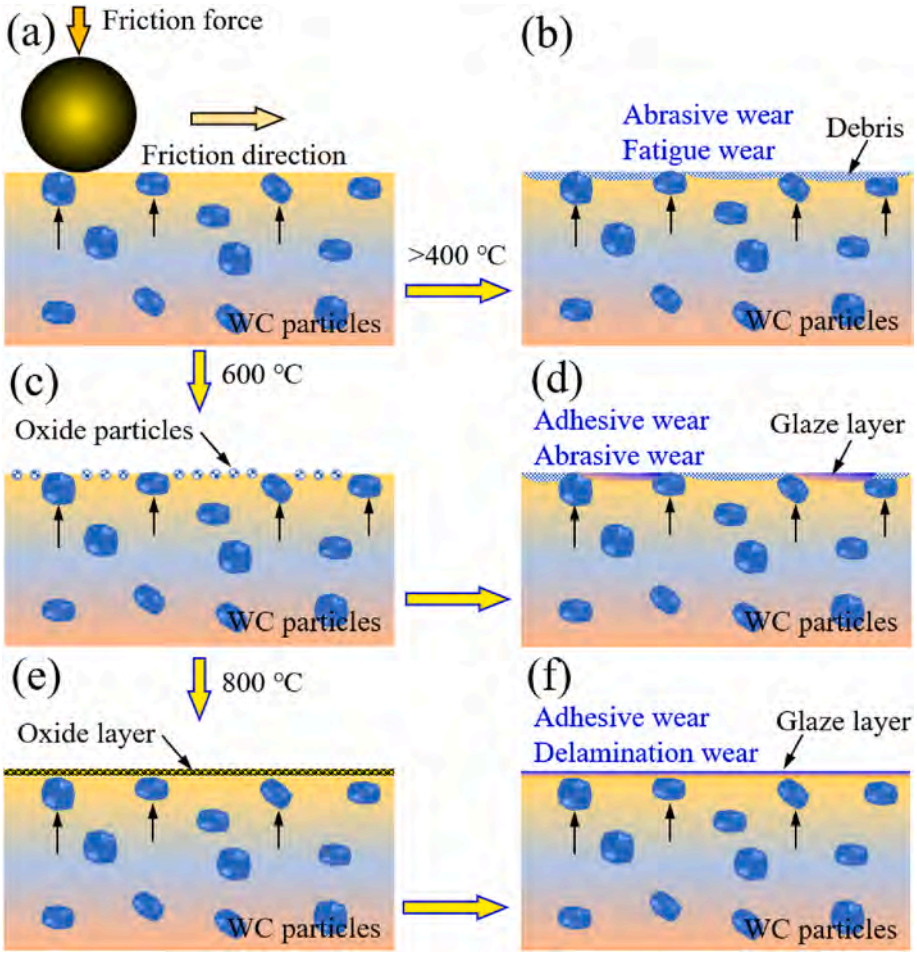

Fig. 14. Schematic diagram of the friction process at different temperatures. (a) Schematic diagram of the friction process, (b) Below 400 °C, (c and d) 600 °C, and (e and f) 800 °C.

1.3×10^{-5} mm^3/N·m at 800 °C. The relative wear resistance is higher by 60.5 %, 298.7 %, and 39.5 % than that at room temperature, 400 °C, and 600 °C, respectively. Combining with WC reinforced HEA composite coatings, a relatively superiority of Fe50Mn30Co10Cr10-15 wt% WC is exhibited in this work. Especially for 800 °C, thus providing the theoretical and experimental basis for liquid die forging.

CRediT authorship contribution statement

Wenxing Wu: Methodology, Investigation. **Hanxia Liu:** Visualization, Methodology, Investigation. **Xuming Jin:** Investigation. **Liangliang Guo:** Investigation. **Tao Zhu:** Software. **Liangbin Hu:** Funding acquisition, Formal analysis. **Chao Yang:** Writing – original draft, Supervision, Conceptualization. **Pinghu Chen:** Conceptualization. **Changjun Qiu:** Writing – original draft, Funding acquisition. **Paul K. Chu:** Writing – review & editing, Funding acquisition.

Data availability

Data will be made available on request.

Declaration of competing interest

The authors declare that they have no known competing financial interests or personal relationships that could have appeared to influence the work reported in this paper.

Acknowledgments

The authors greatly acknowledge the financial support from the National Natural Science Foundation of China (Grant No. 52371032), the National Key Research and Development Program of China (Grant No. 2023YFC3010902), Doctoral research startup fund at the University of South China (Grant No. 5524QD003), the Postdoctoral Fellowship Program of CPSF under Grant Number GZC20231545, China Postdoctoral Science Foundation (2023M742224), Shanghai Post-doctoral Excellence Program (No. 2023440). Liangbin Hu acknowledges the financial support from the Hengyang City research project of the Science and Technology Bureau (Grant No. 202150063472). Paul K. Chu acknowledges the financial support from City University of Hong Kong Donation Research Grants (DON-RMG 9229021 and 9220061). All the authors declare that they have no known competing financial interests or personal relationships that could have appeared to influence the work reported in this paper.

References

[1] T.W.J. Kwok, W. Zhai, W.Y. Peh, M. Gupta, M.W. Fu, B.W. Chua, Squeeze casting for the production of metallic parts and structures, in: F.G. Caballero (Ed.), Encyclopedia of Materials: Metals and Alloys, Elsevier, Oxford, 2022, pp. 87–99.
[2] J. Deng, B. Xie, D. You, L. Wang, X. Wu, G. Liu, J. Liang, Process parameters design of squeeze casting through an improved KNN algorithm and existing data, J. Manuf. Process. 84 (2022) 1320–1330.
[3] B. Zhao, S. Xing, W. Gao, G. Yan, Effect of pressure on the microstructure refinement, solidification mechanism and fracture behavior of wrought Al-Zn-Mg-Cu alloys prepared by squeeze casting, J. Mater. Process. Technol. 324 (2024) 118239.
[4] G. Bi, G.K.L. Ng, K.M. Teh, A.E.W. Jarfors, Feasibility study on the Laser Aided Additive Manufacturing of die inserts for liquid forging, Mater. Des. 31 (2010) S112–S116.
[5] C.Y. Wang, M.S. Sun, C. Yang, H.Y. Wang, J. Wang, L. Mao, Y. Yang, T. Ying, P. K. Chu, X.Q. Zeng, Degradation behavior of pure Mg in the physiological medium and growth mechanism of surface corrosion product films, J. Magnesium Alloys (2024), 10.1016/j.jma.2024.05.012.
[6] D. Wang, L. Du, Y. Liu, Y. Qi, Z. Du, Effects of variable-cavity liquid forging on microstructure and mechanical properties of Mg–Zn–Y–Zr alloy, Mater. Char. 151 (2019) 96–102.
[7] A. Pazhani, M. Venkatraman, M. Anthony Xavior, A. Moganraj, A. Batako, J. Paulsamy, J. Jayaseelan, A. Anbalagan, J. Shanthi Bavan, Synthesis and characterisation of graphene-reinforced AA 2014 MMC using squeeze casting method for lightweight aerospace structural applications, Mater. Des. 230 (2023) 111990.
[8] J. Jiang, L. Kong, Y. Liu, N. Ge, Y. Wang, C. Ding, D. Zou, Effects of heat treatment on microstructure and mechanical properties of squeeze casting AlSi9Mg alloy flywheel housings formed with local supplementary pressure, J. Mater. Res. Technol. 28 (2024) 2430–2441.
[9] H.G. Jeong, J.B. Lee, Crystallization behaviors of Zr–Ti–Cu–Ni–Be BMG sheet fabricated by squeeze-casting method and its micro-scaled forming, J. Alloys Compd. 536 (2012) S86–S90.
[10] C. Yang, Z.M. Sun, C.Y. Wang, A.H. Huang, T. Ying, L.P. Zhou, Z.S. Ye, S. Xiao, P. K. Chu, X.Q. Zeng, A self-sealing and self-healing MAO corrosion-resistant coating on aluminum alloy by in situ growth of $CePO_4/Al_2O_3$, Corros. Sci. 245 (2025) 112706.
[11] C. Yang, C.Y. Wang, Z. Shen, L.P. Zhou, L.Y. Sheng, D.K. Xu, Y.F. Zheng, P.K. Chu, S. Xiao, T. Ying, X.Q. Zeng, Simultaneous improvement of wear and corrosion resistance of microarc oxidation composite coatings on ZK61 Mg alloy by doping with ZrO_2 nanoparticles, J. Mater. Sci. Technol. 224 (2025) 312–327.
[12] C. Yang, T. Ying, A.H. Huang, J. Huang, P.H. Chen, P.K. Chu, X.Q. Zeng, Enhancing the corrosion resistance of MAO coatings on LY12 alloy by in situ co-doping with zinc phosphate and cerium phosphate, Corros. Commun (2025), 10.1016/j.corcom.2024.10.001.
[13] P. Chhabra, M. Kaur, S. Singh, High temperature tribological performance of atmospheric plasma sprayed Cr_3C_2-NiCr coating on H13 tool steel, Mater. Today Proc. 33 (2020) 1518–1530.
[14] A.A. Emamverdian, Y. Sun, C. Cao, C. Pruncu, Y. Wang, Current failure mechanisms and treatment methods of hot forging tools (dies) - a review, Eng. Fail. Anal. 129 (2021) 105678.
[15] M. Hawryluk, Review of selected methods of increasing the life of forging tools in hot die forging processes, Arch. Civ. Mech. Eng. 16 (2016) 845–866.
[16] Y. Wang, Z. Jia, J. Ji, B. Wei, Y. Heng, D. Liu, Determining the wear behavior of H13 steel die during the extrusion process of pure nickel, Eng. Fail. Anal. 134 (2022) 106053.
[17] P. Widomski, M. Kaszuba, D. Dobras, O. Zindulka, Development of a method of increasing the wear resistance of forging dies in the aspect of tool material, thermo-chemical treatment and PVD coatings applied in a selected hot forging process, Wear 477 (2021) 203828.
[18] A. Bjerke, F. Lenrick, S. Norgren, H. Larsson, A. Markström, R. M'Saoubi, I. Petrusha, V. Bushlya, Understanding wear and interaction between CVD α-Al_2O_3 coated tools, steel, and non-metallic inclusions in machining, Surf. Coating. Technol. 450 (2022) 128997.
[19] R. Gao, Y. Huang, X. Zhou, G. Ma, G. Jin, T. Li, H. Wang, M. Liu, Material system and tribological mechanism of plasma sprayed wear resistant coatings: overview, Surf. Coating. Technol. 483 (2024) 130758.
[20] S. Chen, L. Ni, Y. Zhang, Y. Wang, T. Cui, J. Liang, J. Chen, M. Wang, Laser cladding of a novel Fe-based coating with high wear resistance, corrosion resistance and self-lubricating properties, Surf. Coating. Technol. 478 (2024) 130468.
[21] K. Valleti, P. Miryalkar, R.K. L, Efficacy of TiCrN/DLC coatings for service life enhancement of stamping dies, Vacuum 217 (2023) 112534.
[22] A.J. Maskavizan, J.P. Quintana, E.L. Dalibón, A.B. Márquez, S.P. Brühl, S.B. Farina, Evaluation of wear and corrosion resistance in acidic and chloride solutions of Cathodic Arc PVD chromium nitride coatings on untreated and plasma nitrided AISI 4140 steel, Surf. Coating. Technol. 494 (2024) 131476.
[23] N.D. Campos Neto, A.L. Korenyi-Both, C. Vian, S.P. Midson, M.J. Kaufman, The development of coating selection criteria to minimize die failure by soldering and erosion during aluminum high pressure die casting, J. Mater. Process. Technol. 316 (2023) 117954.
[24] T. Varis, J. Lagerbom, T. Suhonen, L. Raami, S. Terho, J. Laurila, P. Peura, P. Vuoristo, Effect of heat treatments on the wear resistance of HVAF and HVOF sprayed tool steel coatings, Surf. Coating. Technol. 462 (2023) 129508.
[25] M. Prithvi Raj, M. Kumar, A. Kumar Pramanick, Microstructure and hardness evaluation of Stellite 6 coating developed on hot forging die steel using gas tungsten arc cladding process, Mater. Today Proc. 66 (2022) 3718–3722.
[26] N. Schalk, M. Tkadletz, C. Mitterer, Hard coatings for cutting applications: Physical vs. chemical vapor deposition and future challenges for the coatings community, Surf. Coating. Technol. 429 (2022) 127949.
[27] P.G. Lashmi, P.V. Ananthapadmanabhan, G. Unnikrishnan, S.T. Aruna, Present status and future prospects of plasma sprayed multilayered thermal barrier coating systems, J. Eur. Ceram. Soc. 40 (2020) 2731–2745.
[28] Y. Yang, R. Jiang, C. Han, J. Chen, H. Li, Y. Wang, J. Tang, H. Zhou, W. Hu, B. Zheng, Z. Liu, C. Song, D. Wang, Frontiers in laser additive manufacturing technology, additive, Manuf. Front. 3 (2024) 200160.
[29] D. Xiang, Y. Liu, T. Yu, D. Wang, X. Leng, K. Wang, L. Liu, J. Pan, S. Yao, Z. Chen, Review on wear resistance of laser cladding high-entropy alloy coatings, J. Mater. Res. Technol. 28 (2024) 911–934.
[30] E. Kaya, Ceramic reinforced composite coatings on cold work tool steel fabricated by wired direct energy deposited plasma, Surf. Coating. Technol. 475 (2023) 130127.
[31] Y. Huang, Y. Hu, M. Zhang, C. Mao, Y. Tong, J. Zhang, K. Li, K. Wang, On the enhanced wear resistance of laser-clad CoCrCuFeNiTix high-entropy alloy coatings at elevated temperature, Tribol. Int. 174 (2022) 107767.
[32] J. Menghani, A. Vyas, P. Patel, H. Natu, S. More, Wear, erosion and corrosion behavior of laser cladded high entropy alloy coatings – a review, Mater. Today Proc. 38 (2021) 2824–2829.

[33] V.M. Gopinath, S. Arulvel, A review on the steels, alloys/high entropy alloys, composites and coatings used in high temperature wear applications, Mater. Today Proc. 43 (2021) 817–823.
[34] A.F.M.M. Hossain, N. Kumar, Microstructure and mechanical properties of a dual phase transformation induced plasticity Fe-Mn-Co-Cr high entropy alloy, J. Alloys Compd. 893 (2022) 162152.
[35] S. Zhou, Q. Zhao, Y. Xia, Y. Ren, H. Huang, X. Huang, J. Qiu, P. Zhu, X. Li, Y. Xie, Temperature dependence of corrosion behavior of a dual-phase Fe50Mn30Co10Cr10 high entropy alloy in supercritical water at 380–650 °C, Corros. Sci. 240 (2024) 112446.
[36] X.F. Wang, Z.P. Wang, Y.L. Bian, Y. Cai, N.B. Zhang, L. Lu, S.N. Luo, Improving ductility and strength of high-entropy alloy Fe50Mn30Co10Cr10 via multi-directional forging and annealing, Mater. Sci. Eng. 915 (2024) 147258.
[37] L. Feng, G. Jin, X. Cui, B. Lu, Z. Dong, Y. Guan, X. Li, X. Yan, M. Liu, Optimizing laser cladding process parameters for transformation-induced plasticity FeMnCoCr high entropy alloy: a multi-objective approach, Surf. Coating. Technol. 495 (2025) 131536.
[38] T. Zhang, R. Xiong, J.W. Bae, P. Asghari-Rad, S.Y. Ahn, H. Peng, Z. Wang, H.S. Kim, Role of carbon on the enhanced strength-ductility synergy in a high-entropy alloy by multiple synergistic strategies, J. Alloys Compd. 1003 (2024) 175698.
[39] K. Wang, X. Yin, H. Lu, Y. Ai, Interface phase and mechanical properties of $(Fe50Mn30Co10Cr10)_{100-x}Al_x$ laser cladding layer with adjustable Al content, Surf. Coating. Technol. 478 (2024) 130488.
[40] J. Geng, X. Yang, G. Wang, M. Yin, J. Li, Y. Li, Effect of TiB_2 content on the microstructure, corrosion behavior, and wear resistance of $(Fe50Mn30Co10Cr10)_{0.8-x}(TiB_2)_xMo_{0.2}$ high-entropy alloy coatings by laser cladding, Surf. Coating. Technol. 496 (2025) 131662.
[41] P. Chen, W. Wu, H. Liu, H. Li, C. Qiu, Metastable FeCrMnCo HEAs with the reinforcement of tungsten carbide fabricated by laser melting: microstructure, mechanical properties and tribological behaviors, Mater. Char. 206 (2023) 113397.
[42] J. Shang, M. Zhang, S. Tan, A. Xie, L. Meng, Y. Zhang, Improved wear and hot melting loss resistance of a vanadium carbide layer prepared on H13 steel, Mater. Lett. 337 (2023) 133967.
[43] W. Wu, C. Qiu, Y. Zhou, M. Yan, Y. Zhang, R. Li, P. Chen, Influence of Co content on cracking behavior and wear resistance of WCp-reinforced $FeCrMnCo_x$ HEAs fabricated by the laser cladding method, Front. Mater. 9 (2022) 811253.
[44] K. Jin, Z. Yang, P. Chen, P. Feng, X. Qiao, Modeling of solidification process during multi-track laser cladding with 3D cellular automata coupling gas-liquid interface tracking and solute suppression nucleation, J. Mater. Process. Technol. 315 (2023) 117927.
[45] Y. Lan, Y. Peng, Y. Zhang, W. Zhang, W. Yang, A. Wang, W. Fan, L. Zhou, Y. Gao, Q. Ma, Effect of solidification behaviors on microstructures and properties of high-entropy alloys coatings by laser melting deposition, Surf. Coating. Technol. 473 (2023) 130028.
[46] G. Li, X. Wei, S. Zhang, Y. Liu, Z. Wang, Dynamic evolution of temperature field, flow field, and solidification behavior during multilayer multitrack laser cladding, Surf. Coating. Technol. 487 (2024) 131010.
[47] S. Fetni, T.M. Enrici, T. Niccolini, H.S. Tran, O. Dedry, L. Duchêne, A. Mertens, A. M. Habraken, Thermal model for the directed energy deposition of composite coatings of 316L stainless steel enriched with tungsten carbides, Mater. Des. 204 (2021) 109661.
[48] B. Gu, H. Zhang, Y. Wang, G. Xu, C. Wang, L. Gao, J. Chu, Y. Yang, Microstructure and corrosion properties of CrMnFeCoNi high entropy alloy coating by temperature field-assisted laser cladding, Surf. Coating. Technol. 494 (2024) 131473.
[49] Z.A. Bello, M. Kang, J.N. Ndumia, C. Geng, A.N. Jibril, Z. Liu, Microstructure and wear behavior of WC-reinforced AlCoCrFeNiSi high entropy alloy coatings prepared by high-velocity arc spraying, Surf. Coating. Technol. 494 (2024) 131421.
[50] K. Yue, L. Wang, Z. Xu, C. Cheng, Y. Wang, Y. Fan, J. Xu, Z. Wang, Z. Chen, Effect of WC content on the microstructure and wear resistance of laser cladding $AlCoCrFeNiTi_{0.5}$ high-entropy alloy coatings, Ceram. Int. 50 (2024) 41515–41526.
[51] Z. Wang, G. Wang, Z. Song, S. Liu, Y. Zhou, X. Qiu, C. Wu, X. Wang, Z. Chen, C. Meng, Microstructure evolution, wear and corrosion behavior of WC reinforced CoCrFeNiMn high-entropy alloy composite coatings by induction cladding, Surf. Coating. Technol. 486 (2024) 130938.
[52] T. Wu, C. Yang, L. Yu, X. Zheng, L. Zhang, Y. Jiang, Y. Xue, Y. Lu, B. Luan, Microstructure characterization and high-temperature wear mechanism of high-entropy alloy matrix composite coating fabricated by laser cladding, Appl. Surf. Sci. 677 (2024) 161032.
[53] D.T. Yu, R. Wang, C.L. Wu, Z.Z. Wang, X.B. Zhao, S. Zhang, C.H. Zhang, X.P. Tao, Wear, corrosion and cavitation erosion behavior of WC-reinforced FeCrNiMnAl ceramic-high entropy alloy composite coatings by laser cladding, Ceram. Int. 50 (2024) 55790–55800.
[54] X. Wang, S. Zhang, F. Zhao, L. Zhang, Z. Wu, Z. Xie, Oxidation corrosion wear and lubricating mechanisms of WC particles reinforced FeCoCrNiMn high-entropy alloys coatings, Ceram. Int. 50 (2024) 31718–31725.
[55] M. Kaba, H.I. Filiz, Z. Cui, M. Baydogan, H. Cimenoglu, A.T. Alpas, Microstructural effects on impact-sliding wear mechanisms in D2 steels: the roles of matrix hardness and carbide characteristics, Wear 538–539 (2024) 205224.
[56] J. Kuai, H. Zhang, Research on generation and polishing mechanisms of nano grain α-Fe2O3 in precision electrolytic in process dressing (ELID) grinding, Procedia Manuf. 37 (2019) 425–430.
[57] D. Zhang, Y. Liu, H. Li, Y. Song, C. Wang, H. Sun, B. Wang, C. Ma, Y. Zheng, High temperature oxidation behavior and microstructure evolution of medium Mn steel, Surf. Interfaces 46 (2024) 104139.
[58] W. Zeng, M. Zhou, M. Yang, R. Qiu, X. Tan, A. Zhou, X. Luo, Influence of manganese content on microstructure, mechanical properties and high temperature oxidation resistance of reduced activation ferritic/martensitic steels, J. Mater. Eng. Perform. 32 (2023) 9765–9776.
[59] Y. Guo, J. Zhao, B. Xu, C. Gu, K. Feng, Y. Wang, Effect of high-temperature oxidation on the subsurface microstructure and magnetic property of medium manganese austenitic steel, J. Alloys Compd. 913 (2022) 165254.
[60] K. Torkashvand, A.I. Encalada, B.C.N.M. de Castilho, M. Gupta, R. Chromik, S. Joshi, High-temperature sliding wear performance of HVAF sprayed WC-based coatings with alternative binders, Wear 538–539 (2024) 205206.
[61] Y. Lian, A. Han, M. Cui, J. Zhang, A novel Co–Cr–Fe–Ni–Mo–Si MPEA-based Laves phase alloy with high strength and high-temperature wear-resistance, J. Mater. Res. Technol. 27 (2023) 1485–1496.
[62] M. Jerroudi, L. Bih, L. Ouachouo, Effect of the manganese-cobalt substitution on the micro-hardness and thermal properties of zinc phosphate glasses, Mater. Today Proc. 58 (2022) 1242–1245.
[63] X. Shang, Y. Liang, P. Wang, Y. Wu, Synergistic mechanism of the fretting wear resistance of Fe_2O_3/Ag nanostructured coatings prepared by sliding friction and magnetron sputtering, Wear 546–547 (2024) 205313.
[64] H.K. Mehtani, M.I. Khan, B.N. Jaya, S. Parida, M.J.N.V. Prasad, I. Samajdar, The oxidation behavior of iron-chromium alloys: the defining role of substrate chemistry on kinetics, microstructure and mechanical properties of the oxide scale, J. Alloys Compd. 871 (2021) 159583.
[65] J.C. Walker, S.R. Saranu, A.H. Kean, R.J.K. Wood, Fe nano-particle coatings for high temperature wear resistance, Wear 271 (2011) 2067–2079.
[66] W. Su, S. Niu, Y. Huang, C. Wang, Y. Wen, X. Li, C. Deng, C. Deng, M. Liu, Friction and wear properties of plasma-sprayed Cr_2O_3–$BaCrO_4$ coating at elevated temperatures, Ceram. Int. 48 (2022) 8696–8705.

Oxidation behavior and failure mechanism of NiCoCrAl eutectic multi-principal element alloys co-doped with Y and Hf at 1100 ℃ and 1200 ℃

Aihui Huang [a], Chao Yang [b,*], Xuanzhen Liu [a], Han Zhang [a], Fangwei Guo [a], Bingnan Qian [c], Jie Lu [a,*], Xiaofeng Zhao [a], Paul K. Chu [d]

[a] Shanghai Key Laboratory of Advanced High-Temperature Materials and Precision Forming, School of Materials Science and Engineering, Shanghai Jiao Tong University, Shanghai, 200240, China

[b] National Engineering Research Center of Light Alloy Net Forming, Shanghai Jiao Tong University, China

[c] National Key Laboratory of Nuclear Reactor Technology, Nuclear Power Institute of China, Chengdu, 610213, China

[d] Department of Physics, Department of Materials Science & Engineering, and Department of Biomedical Engineering, City University of Hong Kong, Tat Chee Avenue, Kowloon, Hong Kong, China

[*] Corresponding authors: Chao Yang (chaoyang0315@163.com); Jie Lu (lu-jie@sjtu.edu.cn)

Section 1 DSC analysis

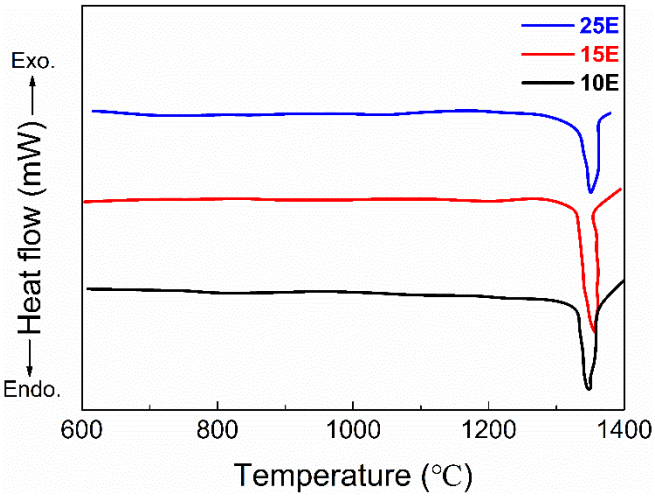

Fig. S1 DSC heat curves of NiCoCrAl EMPEAs, revealing a single endothermic peak during heating.

Section 2 The distribution of Y/Hf-rich precipitates after 100 h oxidation at 1200 ℃

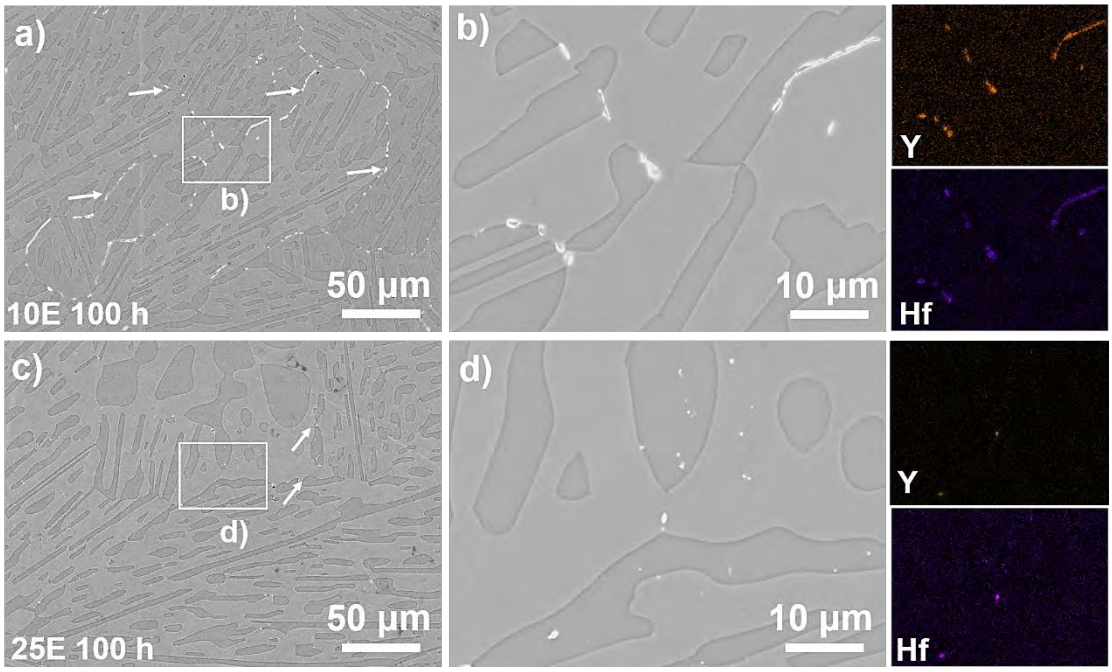

Fig. S2 The microstructure of 10E and 25E alloy after 100 h oxidation at 1200 ℃: a, c) low magnification BSE images, showing the overview of microstructure in 10E and 25E alloys (white arrows indicates the Y/Hf-rich precipitates); b, d) high magnification BSE images and corresponding EDS mapping, showing the detail of Y/Hf-rich precipitates.

Fig. S2 shows the distribution of Y/Hf-rich precipitates in 10E and 25E alloy after 100 h oxidation at 1200 ℃. In the 10E alloy, Y/Hf-rich precipitates are predominantly located at grain boundaries, showing a strong preference on the γ phase. In contrast, the 25E alloy exhibits a more uniform distribution of Y/Hf-rich precipitates across both its γ and β phases, without a notable tendency for aggregation. Furthermore, the phase size of the Y/Hf-rich precipitates in the 25E alloy is significantly larger compared to that in the 10E alloy. These results indicate that the distribution of Y/Hf precipitates plays important role on the difference of oxide intrusions in the NiCoCrAl EMPEAs.

Section 3 The thickness of Al_2O_3 scale after 250 h oxidation at 1200 ℃

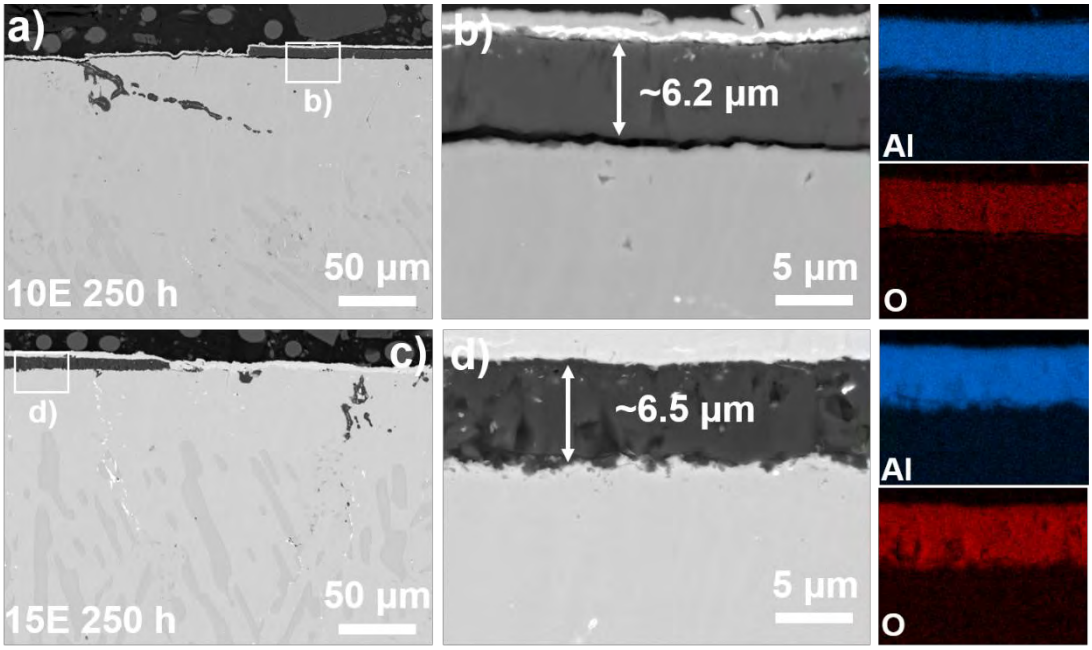

Fig. S3 The cross-sectional morphology of Al_2O_3 scale formed on the 10E and 15E alloys after 250 h oxidation at 1200 ℃: a, c) low magnification BSE images, showing the overview of Al_2O_3 scale; b, d) high magnification BSE images and corresponding EDS mapping, showing the thickness of Al_2O_3 scale.